The Astrophysical Journal, 760:49 (13pp), 2012 November 20 doi:10.1088/0004-637X/760/1/49

LARGE-SCALE STAR-FORMATION-DRIVEN OUTFLOWS AT $1 < z < 2$ IN THE 3D-HST SURVEY

Britt F. Lundgren[1], Gabriel Brammer[2], Pieter van Dokkum[1], Rachel Bezanson[1], Marijn Franx[3], Mattia Fumagalli[3], Ivelina Momcheva[1], Erica Nelson[1], Rosalind E. Skelton[1], David Wake[1], Katherine Whitaker[1], Elizabete da Cunha[4], Dawn K. Erb[5], Xiaohui Fan[6], Mariska Kriek[7], Ivo Labbé[3], Danilo Marchesini[8], Shannon Patel[3], Hans Walter Rix[4], Kasper Schmidt[4], and Arjen van der Wel[4]

[1] Astronomy Department, Yale University, New Haven, CT 06511, USA
[2] European Southern Observatory, Alonso de Córdova 3107, Casilla 19001, Vitacura, Santiago, Chile
[3] Leiden Observatory, Leiden University, NL-2300 RA Leiden, The Netherlands
[4] Max Planck Institute for Astronomy (MPIA), Königstuhl 17, D-69117, Heidelberg, Germany
[5] Department of Physics, University of Wisconsin-Milwaukee, P.O. Box 413, Milwaukee, WI 53201, USA
[6] Steward Observatory, University of Arizona, Tucson, AZ 85721, USA
[7] Department of Astronomy, University of California, Berkeley, CA 94720, USA
[8] Physics and Astronomy Department, Tufts University, Medford, MA 02155, USA
Received 2012 July 24; accepted 2012 September 17; published 2012 November 2

ABSTRACT

We present evidence of large-scale outflows from three low-mass ($\log(M_*/M_\odot) \sim 9.75$) star-forming ($\mathrm{SFR} > 4\,M_\odot\ \mathrm{yr}^{-1}$) galaxies observed at $z = 1.24$, $z = 1.35$, and $z = 1.75$ in the 3D-HST Survey. Each of these galaxies is located within a projected physical distance of 60 kpc around the sight line to the quasar SDSS J123622.93+621526.6, which exhibits well-separated strong ($W_r^{\lambda 2796} \gtrsim 0.8$ Å) Mg II absorption systems matching precisely to the redshifts of the three galaxies. We derive the star formation surface densities from the Hα emission in the WFC3 G141 grism observations for the galaxies and find that in each case the star formation surface density well exceeds $0.1\,M_\odot\ \mathrm{yr}^{-1}\ \mathrm{kpc}^{-2}$, the typical threshold for starburst galaxies in the local universe. From a small but complete parallel census of the $0.65 < z < 2.6$ galaxies with $H_{140} \lesssim 24$ proximate to the quasar sight line, we detect Mg II absorption associated with galaxies extending to physical distances of 130 kpc. We determine that the $W_r > 0.8$ Å Mg II covering fraction of star-forming galaxies at $1 < z < 2$ may be as large as unity on scales extending to at least 60 kpc, providing early constraints on the typical extent of starburst-driven winds around galaxies at this redshift. Our observations additionally suggest that the azimuthal distribution of $W_r > 0.4$ Å Mg II absorbing gas around star-forming galaxies may evolve from $z \sim 2$ to the present, consistent with recent observations of an increasing collimation of star-formation-driven outflows with time from $z \sim 3$.

Key words: galaxies: evolution – galaxies: general – quasars: absorption lines – quasars: general

Online-only material: color figures

1. INTRODUCTION

Outflowing galactic winds have been widely observed in galaxies from $z \sim 6$ to the present and appear to play a fundamental role in galaxy evolution, regulating galactic star formation (e.g., Sanders et al. 1988; Di Matteo et al. 2005; Hopkins et al. 2005) and enriching the intergalactic medium (IGM) at high redshift (e.g., Madau et al. 2001; Scannapieco et al. 2002). However, the enclosed gas mass, physical extent, and physical conditions required to trigger galaxy-scale outflows remain to be better quantified before a complete understanding of the contribution of winds to the observed co-evolution of galaxies and the IGM may be achieved.

Bright, background quasars provide one of the most effective tools for probing the cold gas content of galaxies and their extended halos (e.g., Bahcall & Spitzer 1969), as metal absorption features in quasar spectra have been shown to probe enriched gas in a wide range of galaxy environments, extending to ∼150 kpc around foreground galaxies (e.g., Chen et al. 2010a; Crighton et al. 2010; Steidel et al. 2010; Bordoloi et al. 2011). The low-ionization Mg II doublet (λλ2796, 2803), a tracer of $T \sim 10^4$ K photoionized gas, is particularly prolific, and is observable in the range $0.35 < z < 2.2$ in the optical and across six decades of neutral hydrogen column density (e.g., Churchill et al. 2000). Thus, Mg II provides a common and sensitive probe of the distribution of enriched gas in galaxy halos, capable of tracing the most fundamental disk–halo processes: star-formation-driven outflows and cold-mode accretion.

Despite the fact that tens of thousands of Mg II absorption line systems have been extracted from spectroscopic quasar surveys to date (e.g., Prochter et al. 2006; Quider et al. 2011, D. G. York et al., in preparation), our understanding of the origins and environments of these absorbers remains underdeveloped. This has largely been due to the fact that at the redshifts where Mg II is most easily detected ($z > 0.4$), the individual galactic hosts tend to be too faint or too close to the quasar on the sky to be properly resolved with ground-based observations.

Theoretically Mg II absorption is capable of tracing the interstellar medium of the host galaxy (e.g., Prochaska & Wolfe 1997), star-formation-driven outflows (e.g., Norman et al. 1996; Nulsen et al. 1998), and cold-mode accretion from gas in the extended halos of galaxies (e.g., Kacprzak et al. 2010; Stewart et al. 2011). The currently favored paradigm implies that the absorber rest-frame Mg II equivalent width, W_r (2796 Å), can be used to discriminate between these origins, with the highest equivalent widths being associated with disks and star-formation-driven winds, and the lowest W_r systems indicating more extended, virialized gas.

At intermediate redshifts, the observed anti-correlation between clustering strength (halo mass) and W_r argues against the interpretation that the Mg II absorption systems are virialized (Bouché et al. 2006; Lundgren et al. 2009; Gauthier et al. 2009);

instead, the observed correlation between W_r and star formation rate (SFR) from stacking analyses implies that these systems can be explained by outflowing winds (Zibetti et al. 2007; Noterdaeme et al. 2010; Ménard et al. 2011). This scenario is also consistent with observations of blueshifted Mg II absorption features in the spectra of star-forming galaxies at similar redshifts (Weiner et al. 2009; Rubin et al. 2010; Erb et al. 2012; Martin et al. 2012; Kornei et al. 2012). However, the aforementioned statistical studies of Mg II quasar absorption lines are not based on the direct detection of Mg II absorber host galaxies, and it has been suggested that both the stacking and clustering results could have other explanations (Tinker & Chen 2008; Chen et al. 2010a). Still, the detection of a strong azimuthal dependence of high-W_r Mg II absorption within 50 kpc of disk-dominated galaxies at $z < 1$ has added to the support for an outflow origin (Bordoloi et al. 2011; Bouché et al. 2012a; Kacprzak et al. 2012), given the similar geometry of bipolar outflows observed in local starbursts (e.g., Heckman et al. 1990; Lehnert & Heckman 1996; Cecil et al. 2001; Strickland & Heckman 2009).

A number of studies have used deep imaging or spectroscopy to try to either directly or statistically identify Mg II host galaxies at $z > 0.5$ (e.g., Le Brun et al. 1993; Steidel et al. 1997; Nestor et al. 2007, 2011; Bouché et al. 2007; Straka et al. 2010; Chun et al. 2010) resulting in a few hundred individual detections. While Mg II has been found in association with a wide range of galaxy types, the ultra-strong ($W_r > 2$ Å) absorbers seem to predominantly trace galaxies with high SFRs, at least at high redshift.

However, many galaxy hosts of ultra-strong Mg II remain undetected in even the deepest ground-based data. In the most sensitive survey to date, Bouché et al. (2007) detected just 66% of the host galaxies of ultra-strong Mg II absorbers at $z \sim 1$ using ultra-deep SINFONI IFU observations, and this number dropped to 20% at $z \sim 2$ (Bouché et al. 2012b). These results could indicate that either the Mg II host galaxies have SFRs below the detection limit, are beyond the SINFONI field of view (40 kpc at $z = 1$), or lie too close to the quasar to be detected at ground-based resolution.

In the low-redshift universe ($z \lesssim 0.5$), studies of directly detected Mg II absorber host galaxies have shown that the origins of Mg II are even less clear in the case of the more common population of absorbers with $W_r \lesssim 2$ Å. Analyses of galaxies around detected Mg II absorbers (Kacprzak et al. 2011b) and of the absorption properties of galaxies close to quasar sight lines (Chen et al. 2010a, 2010b) each find an inverse relation between W_r and impact parameter at $z \lesssim 0.4$ with a large (∼1 dex) scatter, which can be reduced by accounting for host galaxy inclination and luminosity. The SFRs of the host galaxies in each study provide little support for models in which winds driven by star formation in the host galaxy produce Mg II absorption with $W_r \lesssim 1$ Å, suggesting that the bulk of Mg II absorbers probes infalling gas from disk–halo processes in normal galaxies.

While much of the evidence described above supports a picture in which high equivalent width Mg II absorbers trace star-forming galaxies at small angular separations from quasar sight lines, the high-W_r systems have typically been studied at high redshift where only the brightest most rigorously star-forming systems are likely to be identified, whereas the local universe studies, which probe galaxies to fainter limits, are statistically restricted to lower W_r systems as well as galaxies with lower average specific SFRs. This potential bias, combined with the uncertainties outlined above, suggests that the interpretation of a correlation between W_r and host SFR requires a deeper examination.

In an effort to begin resolving this problem, we have harnessed the peerless sensitivity and resolving power of the WFC3 G141 grism to study the absorption properties of a complete sample of galaxies surrounding the only known bright $z > 2$ quasar within the 3D-HST Survey (van Dokkum et al. 2011; Brammer et al. 2012). These data enable us to study, for the first time, the properties (redshifts, morphologies, azimuthal angles, SFRs, and stellar masses) of a small but complete sample of Mg II-selected galaxies at $z > 1$. Furthermore, we are also able to study the $W_r > 0.2$ Å absorption properties for a volume-limited sample of galaxies in the foreground of the quasar at virtually unlimited impact parameters ($5 \lesssim \rho$ [kpc] $\lesssim 450$) and to extremely low SFRs ($2\ M_\odot\ \mathrm{yr}^{-1}$), thus eliminating the most prohibitive biases of previous high-redshift studies of the cold gas content of normal galaxies.

The observations contributing to this work are described in Section 2, and details of our analysis are given in Section 3. In Section 4, we present a discussion of the results and their implications with regard to the evolving distribution of Mg II around galaxies from $z \sim 2$. Throughout this paper, we assume a flat Λ-dominated CDM cosmology with $\Omega_m = 0.3$, $H_0 = 70$ km s^{-1} Mpc^{-1}, and $\sigma_8 = 0.8$ unless otherwise stated.

2. OBSERVATIONS

2.1. Galaxy Observations in the 3D-HST Survey

The 3D-HST Survey (van Dokkum et al. 2011; Brammer et al. 2012) is a 600 arcmin^2 survey using the *Hubble Space Telescope* (*HST*) to obtain complete, unbiased low-resolution spectra for ∼7000 galaxies at $1 < z < 3.5$ (Cycles 18 and 19, PI: van Dokkum). The 3D-HST observing strategy employs WFC3 G141 grism observations, paired with WFC3 F140W direct imaging in order to extract a nearly complete census of two-dimensional (2D) spectra for objects in the survey area to a 5σ limiting depth of $H_{140} \sim 26.1$, comparable to the deepest ground-based surveys. Within the 3D-HST Survey, we include data from the A Grism H-Alpha SpecTroscopic (AGHAST[9]) Survey (B. J. Weiner et al., in preparation), an *HST* Cycle 17 program covering GOODS-N with the same depth in G141 and F140W as the larger 3D-HST footprint. It is the observations obtained by the AGHAST survey that specifically contain the quasar sight line examined in this work.

The WFC3 G141 provides slitless spectroscopy over the wavelength range 1.10–1.65 μm with a first-order dispersion of 46.5 Å pixel^{-1} ($R \sim 130$) and a spatial resolution of ∼0.″13, sampled with 0.″06 pixels. These specifications enable the detection of Hα emission in the redshift range $0.7 < z < 1.5$, [O III]λ5007 in the range $1.2 < z < 2.3$, and [O II]λ3727 for $2.0 < z < 3.4$. The grism data have been reduced and analyzed using a variation on the method described in Brammer et al. (2012). This reduction relies on first detecting sources from the F140W imaging, using SExtractor (Bertin & Arnouts 1996). Further care is taken in the grism spectral extraction to reduce contamination from nearby sources and sky background. A complete description of this technique will be presented in G. Brammer et al. (in preparation).

In addition to the WFC3 imaging and grism data, the 3D-HST Survey employs ancillary broadband photometry in

[9] http://mingus.as.arizona.edu/~bjw/aghast/

Table 1
Ancillary Deep Broadband Photometry

Filter(s)	Telescope	Instrument	Observations	Reference
U	KPNO 4 m	MOSAIC	2002 Mar 9–13	Capak et al. (2004)
G	Keck I	LRIS B	2003 Apr 3	Steidel et al. (2003)
Rs	Keck I	LRIS R	2003 Apr 3	Steidel et al. (2003)
B, *V*, *I*, *Z*	*HST*	ACS	*HST* Cycle 12	Giavalisco et al. (2004)
J, *H*, *Ks*	Subaru	MOIRCS	2006–2008	Kajisawa et al. (2011)
F140W	*HST*	WFC3	*HST* Cycle 17	B. J. Weiner et al. (in preparation)
3.6, 4.5, 5.8, 8.0 μm	*Spitzer*	IRAC	2004	Dickinson et al. (2003)

the overlapping fields to determine the broader spectral energy distribution (SED) of each object detected in the WFC3 F140W imaging. In the case of GOODS-N, the ancillary deep broadband imaging ranges from the *U* band through 8 μm, as detailed in Table 1. The aperture photometry, to be described in R. Skelton et al. (in preparation), was performed after matching all images to the point-spread function of the F140W image, using an identical technique as Lundgren et al. (2012). The photometric data provide a means for scaling and tilting the G141 1D spectra, which optimizes the determination of the best-fit redshift and stellar population of each source. The method of fitting the G141 grism redshifts using the EAZY code (Brammer et al. 2008) is described in detail in Brammer et al. (2012).

2.2. Quasar Observations in the SDSS and TKRS

Due to the relatively small area covered by the 3D-HST Survey and the general sparseness of bright quasars, a search for quasars in the Sloan Digital Sky Survey (SDSS; York et al. 2000) DR7 quasar catalog (Schneider et al. 2010) within the 3D-HST footprint produced only one quasar: SDSS J123622.93+621526.6, with $z = 2.5946$ and $m_r = 20.4$. A $20'' \times 20''$ WFC3 F140W image from program GO-11600 of the field around this quasar is presented in Figure 1. The exceptional gain in resolution and depth of the WFC3 imaging in comparison to high-resolution ground-based imaging is illustrated by the $8'' \times 8''$ *R*-band image from Keck II (Wirth et al. 2004), shown as an inset to the figure.

The signal-to-noise ratio (S/N) per resolution element of the SDSS DR7 spectrum of SDSS J123622.93+621526.6 is ~3, which at the typical SDSS resolution of $R = 1800$ (Uomoto et al. 1999) is sufficient only for detecting absorption features with $W_r \gtrsim 1.5$ Å at 3σ significance. As the Mg II equivalent width distribution function (dN/dW) in the SDSS is steep (Nestor et al. 2005), most Mg II absorbers have $W_r < 1$ Å. We therefore required a greater depth than the limiting equivalent width of the SDSS observation in order to undertake a more comprehensive analysis of the foreground absorption in this particular quasar spectrum.

A higher signal-to-noise spectrum of this quasar is publicly available as part of the Team Keck Treasury Redshift Survey (TKRS; Wirth et al. 2004), a deep imaging and spectroscopic survey in the GOODS-N field using the Deep Imaging Multi-Object Spectrograph (DEIMOS; Faber et al. 2003) on the Keck II telescope. The TKRS contains spectra of 1440 galaxies and active galactic nuclei (AGNs), with wavelength coverage from 4600 to 9800 Å and an FWHM resolution of $\Gamma \approx 3.5$ Å. Each slit mask acquired an on-source integration time of 3600 s, resulting in a mean per pixel S/N of 11.7 for the quasar examined in this work (TKRS GOODS-N ID: J123622.94+621527.0). Though the DEIMOS resolution is slightly worse than that of the SDSS, the higher S/N enabled detection of absorption at the lower observed equivalent width limit of $W_r > 0.2$ Å. The measurements included in this paper have therefore all been determined using the TKRS DEIMOS spectrum.

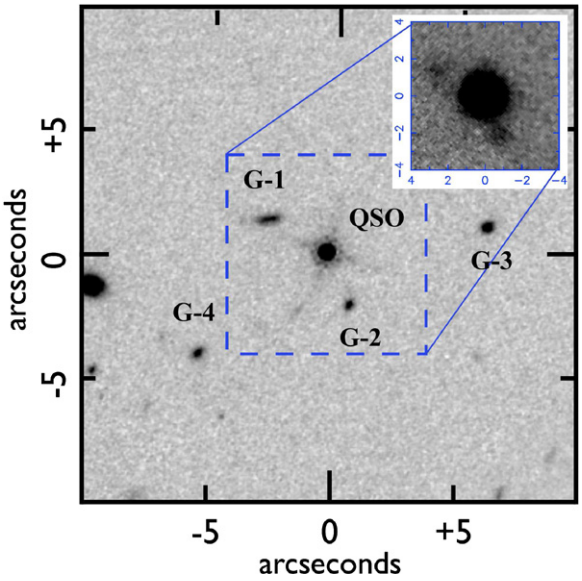

Figure 1. $20'' \times 20''$ cutout of a WFC3 F140W image from the AGHAST GOODS-N *HST* grism program (B. J. Weiner et al., in preparation), centered on the $m_r = 20.4$ quasar SDSS J123622.93+621526.6 with $z = 2.59$. Each of the four galaxies identified within 60 kpc of the quasar sight line are labeled G-1−G-4. Inset is an $8'' \times 8''$ DEIMOS *R*-band image from the Team Keck Treasury Redshift Survey (TKRS; Wirth et al. 2004), illustrating the difficulty of using ground-based observations to obtain redshifts of faint galaxies with small angular separations around even this reasonably faint background quasar.
(A color version of this figure is available in the online journal.)

3. ANALYSIS

3.1. Identification of Quasar Absorption Lines

With the aim of producing a complete set of metal absorption lines in the spectrum of quasar SDSS J123622.93+621526.6, we apply an automated approach similar to the pipeline used to extract metal absorption lines from the SDSS DR7 (York et al. 2005; Lundgren et al. 2009; D. G. York et al., in preparation). This approach fits a pseudocontinuum to the quasar spectrum using a moving average with an adaptive smoothing length that depends on the proximity to emission lines in the quasar spectrum. This technique reliably fits the shape of quasar continua for a wide range in spectral morphologies, with the exception of broad absorption line quasars and regions of the Lyα forest.

After normalizing the DEIMOS spectrum by the determined continuum, residual narrow absorption features are fitted with a

Table 2
Ions Detected in Absorption along the Quasar Sight Line

z_{abs}	λ_{obs} (Å)	W_r (Å)	σ_{W_r} (Å)	λ_r (Å)	Ion	Δz[a]
1.2408	5339.77	0.49	0.06	2382.8	Fe II	−0.0002
	5826.46	0.24	0.05	2600.2	Fe II	0.0000
	6265.85	0.79	0.08	2796.4	Mg II	0.0001
	6281.61	0.80	0.07	2803.5	Mg II	0.0001
1.3579	5522.89	0.09	0.03	2344.2	Fe II	0.0019
	5600.13	0.18	0.04	2374.5	Fe II	−0.0006
	5618.17	1.33	0.07	2382.8	Fe II	0.0001
	5856.37	0.15	0.05	2484.0	Fe I	0.0003
	6099.43	0.65	0.09	2586.7	Fe II	−0.0001
	6130.74	1.28	0.08	2600.2	Fe II	0.0001
	6592.84	2.64	0.07	2796.4	Mg II	0.0003
	6609.79	2.51	0.08	2803.5	Mg II	0.0002
1.7444	5562.73	0.33	0.03	2026.5	Mg I	−0.0006
	6433.55	0.41	0.05	2344.2	Fe II	−0.0001
	6539.17	0.73	0.07	2382.8	Fe II	0.0001
	7072.05	0.13	0.03	2576.9	Mn II	0.0000
	7098.18	0.31	0.05	2586.7	Fe II	0.0003
	7135.74	0.72	0.07	2600.2	Fe II	0.0001
	7673.88	1.82	0.09	2796.4	Mg II	0.0002
	7693.96	1.32	0.08	2803.5	Mg II	0.0000
0.8306[b]	5118.97	0.24	0.06	2796.4	Mg II	···
0.8552[b]	5187.75	0.28	0.10	2796.4	Mg II	···

Notes.
[a] The difference between the average systemic redshift of absorption lines with 4σ detections, z_{abs}, and the redshift determined for each individual ion, z_{ion}.
[b] Cases in which the equivalent width of Mg II (λ2796) falls below the 4σ criterion for independent detection of a reliably identified absorption system. These absorption features have been measured after first detecting a galaxy with a precise grism redshift and an impact parameter <150kpc.

Gaussian function to calculate the equivalent width and accompanying error of each line. All absorption features with a detection significance $W_r/\sigma_{W_r} \geqslant 3$ are retained for identification. As the doublets of Mg II (λλ2796, 2803) and C IV (λλ1548, 1551) are prolific in optical spectra over a wide range in redshift and also easily identified by their wavelength separation and doublet ratio, these lines are the first target of our automated line identification algorithm. After producing a list of candidate doublets from the detected lines, we then determine the redshift of each doublet and proceed to search for other common line transitions detected in absorption within 150 km s^{-1} of the same redshift.

In quasar SDSS J123622.93+621526.6, this automated line detection algorithm identifies three absorption systems with detections of Mg II doublets and two or more additional accompanying metal transitions with redshifts matching to within 150 km s^{-1}. The redshifts of the absorption line systems ($z = 1.2408, 1.3579, 1.7444$) are determined by averaging the individually determined redshifts of all ions detected in absorption with $W_r/\sigma_{W_r} \geqslant 4$. A full listing of the absorption line measurements is provided in Table 2.

3.2. Analysis of Proximate Galaxies

Having identified all significant absorption features along the line of sight to our central quasar, we next examine the WFC3 F140W and G141 observations to identify all galaxies with $0.65 < z < 2.6$ in the surrounding field. The applied redshift limitations correspond to the range in which emission from either Hα or the [O III]/Hβ complex is observable in the G141. Although the 5σ depth of the F140W images extends to $H_{140} \sim 26$, the continuum limit at which grism redshifts may be reliably obtained for galaxies at $1 < z < 3$ in the 3D-HST Survey effectively limits our search to galaxies with $H_{140} \lesssim 24$ (Brammer et al. 2012). We stress that in this search we pay no regard to the absorption properties of the galaxies. *Thus, our analysis can be used interchangeably as a galaxy-blind survey of absorbers with $W_{obs} > 0.4$ Å as well as an absorption-blind survey of galaxies with* $\log(M_*/M_\odot) > 9$.

To our detection limits, eight galaxies are identified within 150 kpc of the quasar sight line, four of which are detected with projected physical separations of less than 60 kpc (see Table 3). Three of these four closest galaxies exhibit strong emission lines in the extracted one-dimensional (1D) spectra from the G141 grism observations, enabling their redshifts to be precisely determined at $z = 1.238$, $z = 1.357$, and $z = 1.748$. In each of these cases, multiple emission lines are detected in the G141 spectra, ensuring that these redshifts are unambiguous. Equivalent width measurements of the Hα, Hβ, and [O III] emission lines, where observable, are presented in Table 4.

The extracted G141 1D spectra of these three galaxies are presented in Figure 2, with labels G-1−G-3, matching the labels in the F140W image from Figure 1. In each case, the galaxy emission redshift is found to precisely match the redshift of one of the separately identified absorption systems detected in the quasar spectrum. Beneath each grism observation in Figure 2, we present a cutout from the TKRS DEIMOS quasar spectrum, centered on the detected doublet of Mg II absorption matching the redshift of the galaxy separately observed in emission. The difference between the emission and absorption redshifts is $\Delta z/(1+z) \leqslant 0.0015$ in each case, indicative of the precision of grism redshifts among star-forming galaxies in the 3D-HST Survey.

3.2.1. Redshift Precision

As demonstrated in Brammer et al. (2012), the typical precision of 3D-HST galaxy redshifts obtained using the combination of G141 and broadband aperture photometry is $\Delta z/(1+z) = 0.0035$ at $z > 0.7$, approximately one order of magnitude higher than redshifts determined from well-sampled broadband SEDs (Brammer et al. 2008). The precision of the 3D-HST method is also known to increase with the strength and number of emission lines in each G141 spectrum. For example, galaxies with Hα detections with S/N > 5 have a typical 3D-HST redshift precision of $\Delta z/(1+z) = 0.0018$.

Within our sample of eight galaxies, only the three previously mentioned exhibit multiple strong emission lines in the G141 spectra. In three of the five remaining galaxies (G-5, G-7, and G-8), we detect a single emission line with an S/N in the range 2–8, as presented in Table 4. In each of these cases, the 3D-HST redshift estimate is consistent ($0.0006 \leqslant \Delta z/(1+z) < 0.02$) with available spectroscopic redshifts from the GOODS-N catalog of Barger et al. (2008). Neither of the two remaining galaxies (G-4 and G-6) exhibit detectable emission in the G141 spectra. In such cases, the redshift probability distribution, $P(z)$, which is output from the fitting procedure, provides a useful estimate of the redshift precision. The $P(z)$ for each of the two remaining galaxies is narrowly peaked, with an FWHM implying $\Delta z/(1+z) < 0.02$.

3.2.2. Morphologies

The high resolution and small native pixel scale ($0\farcs06$ pixel^{-1}) of the WFC3 F140W images further enable us to examine the

Table 3
Galaxies Identified in 3D-HST within 150 kpc of the Quasar Sight Line

ID	3D-HST[a]	R.A. (deg)	Decl. (deg)	z_{gal}[b]	Sep ($''$)	ρ (kpc)	$(z_{gal}-z_{abs})$	A_v (mag)	$\log(M_*)$[c] ($M_\odot$)	$\log(SFR)$[c] ($M_\odot$ yr^{-1})
G-1	10245	189.09701171	62.25773284	1.357	2.72	23	−0.001	0.9	10.0 ± 0.1	1.20 ± 0.12
G-2	10167	189.09505985	62.25677527	1.748	2.30	20	0.004	0.5	9.4 ± 0.1	1.22 ± 0.13
G-3	10225	189.09169228	62.25763867	1.238	6.62	55	−0.003	0.5	9.5 ± 0.1	1.28 ± 0.05
G-4	10138	189.09873233	62.25622073	0.952	6.67	53	···	0.4	9.1 ± 0.1	0.33 ± 0.14
G-5	10007	189.10030524	62.25449792	0.827	12.98	99	−0.004	0.4	9.3 ± 0.2	0.33 ± 0.05
G-6	09913	189.10052481	62.25325999	0.853	16.92	130	−0.002	0.1	10.1 ± 0.1	-0.92 ± 0.05
G-7	10021	189.10602084	62.25540397	0.659	18.83	131	···	0.2	10.1 ± 0.2	0.56 ± 0.05
G-8	10152	189.10132430	62.25699568	0.683	9.68	69	···	0.9	10.7 ± 0.1	0.15 ± 0.05

Notes.
[a] The unique 3D-HST identification number, which formally includes a prefix of "GOODS-N-14-" referring to the field and pointing.
[b] The 3D-HST redshift estimate, which has been determined using a combination of deep broadband photometry and G141 1D spectra, as described in Brammer et al. (2012). The typical redshift precision is $\Delta z/(1+z) = 0.0035$.
[c] Stellar masses and SFRs estimated assuming the best-fit G141 redshift and SPS modeling of SEDs with 11–15 broadband flux measurements. The SPS modeling assumes a Salpeter (1955) initial mass function and stellar population models from Bruzual & Charlot (2003). The quoted error estimates are derived exclusively from the photometric uncertainties and do not account for the larger systematic uncertainties from the choice of SPS model or initial mass function.

Table 4
Galaxy Emission Line Measurements in G141

ID	z_{gal}	$W_r(H\beta)$ (Å)	$W_r([O\,III])$ (Å)	$W_r(H\alpha)$ (Å)	$F(H\alpha)$ (10^{-17} erg s^{-1} cm^{-2})	SFR($H\alpha$) ($M_\odot$ yr^{-1})	ΣSFR($H\alpha$) ($M_\odot$ yr^{-1} kpc^{-2})
G-1	1.357	7 ± 13	19 ± 22	206 ± 29	8.3 ± 0.9	7.3 ± 0.8	0.37 ± 0.05
G-2	1.748	189 ± 33	537 ± 57	···	···	···	···
G-3	1.239	1 ± 4	43 ± 13	159 ± 14	6.5 ± 0.5	4.6 ± 0.4	0.98 ± 0.12
G-4	0.952	···	···	<6	···	···	···
G-5	0.827	···	···	97 ± 50	4.7 ± 2.5	1.2 ± 0.7	0.02 ± 0.01
G-6	0.853	···	···	<6	···	···	···
G-7	0.659	···	···	79 ± 35	17 ± 8	2.4 ± 1.2	0.05 ± 0.02
G-8	0.683	···	···	73 ± 9	23 ± 3	3.7 ± 0.5	0.16 ± 0.02

Table 5
Galaxy Morphological Parameters in F140W

ID	m_{F140}	R_e[a] (pixel)	$R_{e,c}$[b] (kpc)	n[c]	b/a	P.A. (deg)	Φ[d] (deg)
G-1	23.15	6.4 ± 0.3	1.8 ± 0.1	0.5 ± 0.1	0.26 ± 0.01	69 ± 1	37 ± 2
G-2	23.93	2.2 ± 0.3	0.7 ± 0.1	1.8 ± 0.5	0.33 ± 0.05	-50 ± 3	46 ± 14
G-3	23.07	1.9 ± 0.1	0.9 ± 0.1	2.7 ± 0.4	0.68 ± 0.05	88 ± 6	17 ± 6
G-4	23.59	2.8 ± 0.1	1.2 ± 0.1	1.0 ± 0.2	0.63 ± 0.04	-69 ± 5	···
G-5	23.35	7.4 ± 0.7	2.8 ± 0.4	0.9 ± 0.1	0.60 ± 0.04	-22 ± 6	···
G-6	22.45	1.7 ± 0.1	0.7 ± 0.1	7 ± 1	0.74 ± 0.04	-16 ± 5	···
G-7	21.64	9.0 ± 0.3	2.7 ± 0.1	1.7 ± 0.1	0.43 ± 0.01	-4 ± 1	···
G-8	21.33	4.9 ± 0.1	1.9 ± 0.1	0.8 ± 0.1	0.71 ± 0.01	32 ± 1	···

Notes.
[a] R_e indicates the effective radius of the galaxy light profile along the semimajor axis.
[b] The circularized effective radius, $R_{e,c} = R_e\sqrt{b/a}$, where (b/a) is the axis ratio, provided in the fifth column of the table.
[c] The Sérsic index, estimated using the *GALFIT* software (Peng et al. 2002).
[d] Azimuthal angle to the quasar sight line.

morphologies of the galaxies proximate to the quasar sight line. Using the *GALFIT* software package (Peng et al. 2002), we derive the effective radius (R_e), Sérsic index, axis ratio (b/a), and position angle (P.A.) for each of the eight galaxies identified within 150 kpc of the quasar sight line. These measurements and errors, both from *GALFIT*, are presented in Table 5.

From the measured position angles, we also calculate the azimuthal angle, Φ, for each galaxy, relative to the quasar. We define this angle using the same convention as Bouché et al. (2012a) and Kacprzak et al. (2012), in which Φ refers to the angle produced by the major axis of the galaxy and the vector relating the center of the galaxy to that of the quasar. For cases in which the quasar is aligned with the major axis of the galaxy $\Phi = 0^\circ$, and $\Phi = 90^\circ$ when the quasar aligns with the minor axis of the galaxy.

The slitless nature of the WFC3 grism also enables the extraction of 2D emission line maps, as recently demonstrated by Nelson et al. (2012). We use the same technique of fitting and

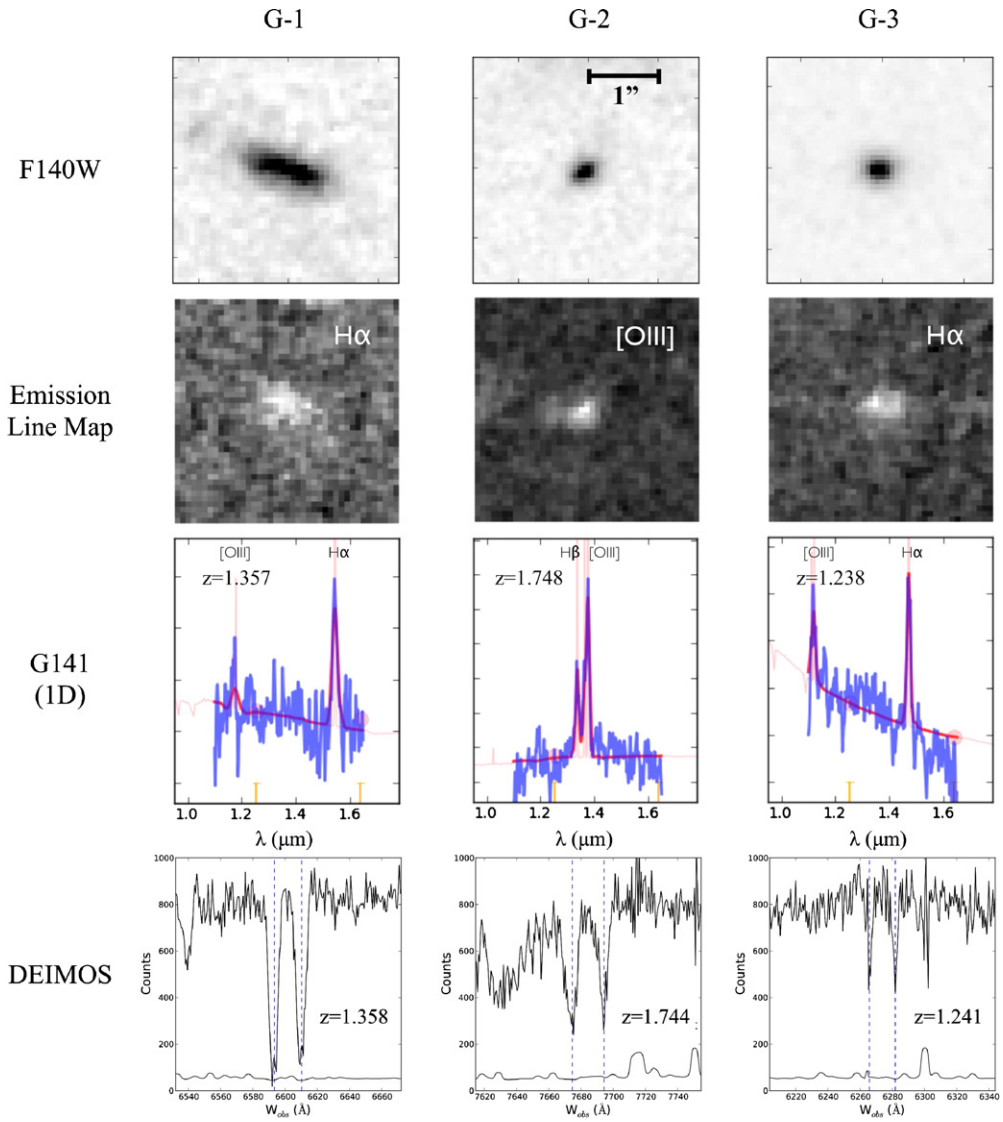

Figure 2. Top row: WFC3 F140W 2″ × 2″ imaging cutouts for each of the three star-forming galaxies labeled in Figure 1 as G-1, G-2, and G-3. For physical scale, 1″ is equivalent to 8.5 kpc at the mean redshift of this sample, $z = 1.44$. Second row: emission line maps for each galaxy, produced using a combination of the WFC3 F140W imaging and G141 2D grism data. Third row: WFC3 G141 1D grism observations are shown in blue with a best-fit template galaxy spectrum overlaid in red. Best-fit redshifts are inset. Bottom: the corresponding three portions of the KTRS DEIMOS spectrum and 1σ error array of the nearby quasar SDSS J123622.93+621526.6, in which an Mg II absorption doublet is detected with a redshift consistent with that of each galaxy in WFC3 G141, at projected separations of <60 kpc. The grism redshift of each galaxy precisely matches the mean redshift of a detected Mg II absorption line system with $\Delta z/(1+z) \leqslant 0.0015$.

(A color version of this figure is available in the online journal.)

subtracting the 1D continuum emission, row by row, from the 2D spectrum to produce emission line maps for the three galaxies closest to the quasar sight line. Such maps for the three galaxies observed in absorption at $z > 1$ are provided in Figure 2. For the two galaxies with observable Hα in the G141 spectrum we find that the resolved emission line regions are extended, allowing us to rule out a dominant flux contribution from an AGN in each case. We note that the Hα emission generally traces the rest-frame optical morphology of each galaxy, consistent with the findings of Nelson et al. (2012).

3.2.3. Stellar Population Estimates

For each of the galaxies with Hα emission line measurements in the G141 spectra we estimate the SFR using the relation from Kennicutt (1998):

$$\mathrm{SFR}(\mathrm{H}\alpha)\ [M_\odot\ \mathrm{yr}^{-1}] = 7.9 \times 10^{-42} \times L(\mathrm{H}\alpha)\ [\mathrm{erg\ s}^{-1}] \quad (1)$$

and present the measurements in Table 4. We apply no correction for dust extinction, so these estimated SFRs should be understood as lower limits of the true SFR.

For galaxies in which strong emission lines are not evident or observable in the G141 1D spectra, ancillary multi-band photometric observations facilitate the estimation of the stellar masses and SFRs from stellar population synthesis (SPS) modeling. The stellar masses and SFRs, estimated from the SED of each galaxy alone, are given in Table 3. These estimates are obtained using the FAST code (Kriek et al. 2009), assuming a Salpeter (1955) initial mass function and the stellar population models of Bruzual & Charlot (2003) with solar metallicity. In estimating the SFRs, we apply the recommended prescriptions of Wuyts et al. (2011), requiring an exponentially declining (τ model) star formation history and a minimum e-folding time of $\log(\tau_{\mathrm{min}}[\mathrm{yr}]) = 8.5$, as these constraints have been shown to best reproduce low-to-intermediate SFRs within the Bruzual & Charlot (2003) framework. For the estimation of stellar masses

we allow more freedom in the best-fit SPS models, setting $\log(\tau_{\rm min}[{\rm yr}]) = 7$ (see also Lundgren et al. 2012, submitted).

We note that the SFR estimates derived from SPS modeling from FAST are consistently >2 times larger than the SFRs extracted from the Hα emission line measurements. This difference, which is consistent with the findings of Nelson et al. (2012), can be attributed to the fact that the SPS modeling simultaneously fits for dust extinction, whereas a similar correction has not been made to the SFRs derived from Hα emission in the grism data.

Using the Hα-derived SFRs when available, we calculate the average star formation surface density, ΣSFR, as

$$\Sigma{\rm SFR}\ [M_\odot\ {\rm yr}^{-1}\ {\rm kpc}^{-2}] = 0.5 \times {\rm SFR}/\pi R_{e,c}^2, \quad (2)$$

where $R_{e,c}$ is the circularized effective radius of the galaxy in the F140W image, defined as

$$R_{e,c} = R_e\sqrt{b/a}. \quad (3)$$

Here, R_e is the effective radius along the semimajor axis measured in kpc, and (b/a) is the axis ratio, described in Section 3.2.2 and presented in Table 5. While circularizing the effective radius would be inappropriate for thin disks, in which inclination has a large effect on the measured surface area, we find it to be a safe approximation for the more elongated, irregular, and puffy morphologies of the galaxies in our analysis.

4. DISCUSSION

Our essentially unbiased search for the galaxy hosts of Mg II absorption with $W_r^{\lambda 2796} > 0.4$ Å in the 3D-HST Survey area produces a 100% detection rate in the available redshift range of the G141 grism. In each case, the Mg II host galaxy is located within 60 kpc of the quasar sight line and has resolved emission lines and SEDs implying SFRs $> 4\ M_\odot\ {\rm yr}^{-1}$. All of the galaxies appear to be isolated with no evidence of recent disruption. Thus, there is also no ambiguity in the absorber–galaxy pairing due to multiple candidate galaxy hosts at similar redshifts.

4.1. Properties of Mg II Host Galaxies

For the three galaxies at $z > 1$ exhibiting strong Mg II absorption in the quasar spectrum, we measure effective radii along the semimajor axis ranging from 1 to 3 kpc and Sérsic indices ranging from $0.5 \lesssim n \lesssim 2.7$. We note that the true uncertainties in the structural parameter estimates are larger than those reported by *GALFIT* (e.g., Häussler et al. 2007). If we assume that our small but randomly selected sample is representative of the larger Mg II host galaxy population at $1 < z < 2$, our data suggest that Mg II traces compact, triaxial systems (e.g., G-2, G-3) and thick disks (e.g., G-1), each of which appear to be common among low-mass ($\log(M_*/M_\odot) \lesssim 10$) galaxies at $z \sim 2$ (e.g., Conselice et al. 2005; Elmegreen et al. 2005; Elmegreen & Elmegreen 2006; Ravindranath et al. 2006; Genzel et al. 2006, 2008; Law et al. 2012a).

The two Mg II host galaxies for which Hα is observable in the G141 spectrum (G-1 and G-3) exhibit SFRs in the range 4–8 $M_\odot\ {\rm yr}^{-1}$ and star formation surface densities in the range 0.3–1.0 $M_\odot\ {\rm yr}^{-1}\ {\rm kpc}^{-2}$. Even without applying a dust correction, which would effectively raise the SFRs, we measure a ΣSFR for each galaxy that is well above the threshold over which large-scale outflows are observed in local starburst galaxies and Lyman break galaxies at $z > 2$ ($0.1\ M_\odot\ {\rm yr}^{-1}\ {\rm kpc}^{-2}$; Heckman 2002). Given that outflow velocities exhibit a stronger correlation with ΣSFR than with SFR (Kornei et al. 2012), it is perhaps not surprising that we find evidence of winds extending to large scales around each of these galaxies. If we assume a wind velocity of 400 km s^{-1}, typical of the observations of star-formation-driven winds at $z \sim 1.4$ (Weiner et al. 2009), the impact parameters of the galaxies with respect to the quasar sight line imply that the winds were launched at least ∼50 and ∼150 Myr earlier. The fact that each of the galaxies is still forming stars at a high rate suggests that we may be observing a prolonged burst of star formation on these same timescales.

SED modeling of the galaxy G-2, which is observed in absorption but at too high a redshift for Hα detection in the G141 spectrum, indicates an SFR approximately equal to that of G-1 and G-3. We therefore estimate the ΣSFR to be $\sim 2\ M_\odot\ {\rm yr}^{-1}\ {\rm kpc}^{-2}$, again well above the same starburst threshold. The [O III]/Hβ ratio for this galaxy from the G141 1D spectrum is measured to be $2.8\pm^{1.0}_{0.7}$, consistent with a normal star-forming galaxy. As shown in Figure 2, the resolved [O III] emission is extended, tracing the rest-frame optical morphology and thus disfavoring a dominant flux contribution from an AGN.

The three Mg II host galaxies we detect at $1 < z < 2$ have a mean stellar mass of $\log(M_*/M_\odot) = 9.75$. Using the relation between stellar mass and halo mass in this redshift range from Wake et al. (2011), this corresponds to a dark matter halo mass of $\log(M_h/M_\odot) \sim 11.9$. We therefore find results consistent with the typical $W_r > 0.8$ Å Mg II halo mass derived from clustering measurements at $z \sim 1$, $1.8\pm^{4.2}_{1.6} \times 10^{12}\ M_\odot$ (Lundgren et al. 2011). This value is also consistent with multiple clustering measurements at $z \sim 0.6$ (Bouché et al. 2006; Lundgren et al. 2009; Gauthier et al. 2009), indicating that Mg II host galaxies occupy similarly massive halos at all redshifts $z \lesssim 2$.

Despite our unavoidably small sample, a 100% detection rate of star-forming galaxy hosts of $W_r^{\lambda 2796} > 0.8$ Å Mg II absorption at $z > 1$ is interesting given the results from recent ground-based analyses, which have reported a large fractional absence of strong Mg II host galaxy detections to sensitive limits in the same redshift range. A search for the galactic counterparts of 20 ultra-strong ($W_r^{\lambda 2796} > 2$ Å) Mg II absorbers at $z = 2$ using SINFONI undertaken by Bouché et al. (2012b) had only 20% success in identifying absorber host galaxies, at a reported SFR sensitivity limit of $2.9\ M_\odot\ {\rm yr}^{-1}$. This detection rate represents a drop from 66% at $z \sim 1$ with a similar search (Bouché et al. 2007). The SINFONI field of view limits a search for companions at $z = 2$ to impact parameters less than ∼40 kpc, but the substantial observational evidence indicating that ultra-strong Mg II absorbers are restricted to small impact parameters implies that the missing galaxies are not simply beyond the field of view. Bouché et al. (2012b) also rule out scenarios in which the galaxy hosts are obscured by the quasar at very small impact parameters. Thus, the authors hypothesize that the SFRs of $W_r > 2$ Å Mg II host galaxies may be substantially lower than expected at $z \sim 2$, causing them to lie below the detection threshold of the survey.

The strongest Mg II absorber in our sample (G-1, $z = 1.357$) meets the definition for ultra-strong absorbers studied in the analyses of Bouché et al. (2007, 2012b). With a projected separation of 23 kpc and an SFR $\sim 7\ M_\odot\ {\rm yr}^{-1}$, the host galaxy we detect is also within the field of view and SFR limitations of SINFONI observations and would most certainly have been detected by the Hα surveys of Bouché et al. The second-strongest absorber in our sample (G-2, $z = 1.748$) has an Mg II equivalent width of $W_r = 1.82 \pm 0.09$ Å, slightly weaker than the classic definition of ultra-strong Mg II. Still,

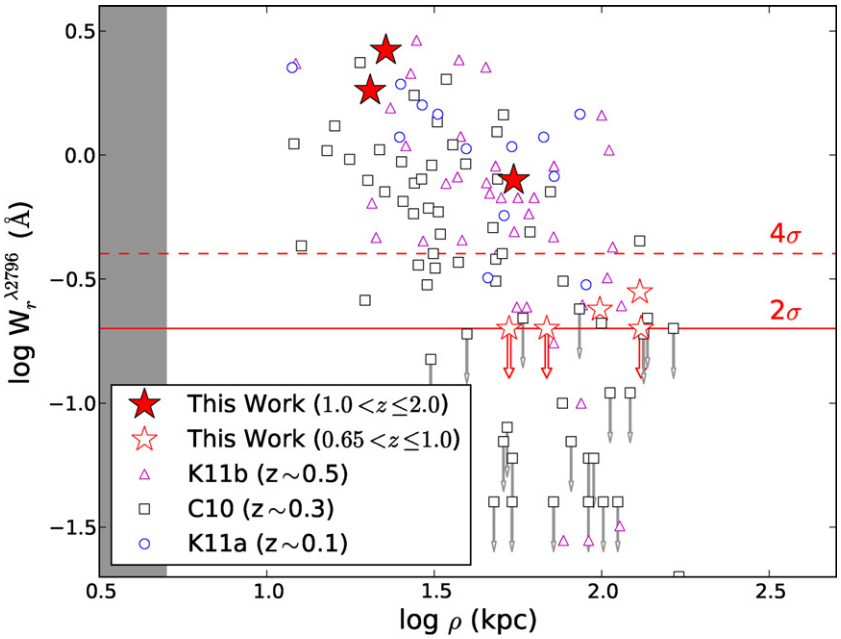

Figure 3. Observed relation between the rest-frame equivalent width of Mg II absorption, $W_r^{\lambda 2796}$, and galaxy impact parameter, ρ, in this work and from the largest existing surveys. Measurements from the literature are overplotted for comparison at low and intermediate redshift (circles, Kacprzak et al. 2011a; squares, Chen et al. 2010a; triangles, Kacprzak et al. 2011b). The shaded gray region indicates the limiting observable impact parameter for this work. Red horizontal lines provide the significance of absorption line detection in the DEIMOS quasar spectrum we examine.

(A color version of this figure is available in the online journal.)

the projected separation between the host galaxy and the quasar sight line is 20 kpc, which is again well within the SINFONI field of view, and the estimated SFR is also above the detection threshold of the SINFONI observations. While our success rate at detecting these host galaxies at small impact parameters hints at a contradiction with the low detection rates from Bouché et al., a sample of two objects cannot provide optimal constraints on the typical SFRs of Mg II host galaxies at $z > 1$. A greater number of G141 observations centered on quasar sight lines with high-redshift Mg II absorption would be required to better examine whether lower-than-predicted SFRs can account for the large number of host galaxies undetected in other surveys.

While this work is primarily focused on galaxies with $z > 1$, we identify two galaxies at lower redshift with impact parameters of ∼100 kpc (G-5, $z = 0.827$; G-6, $z = 0.853$) and corresponding 3σ detections of Mg II with $W_r \sim 0.25$ Å. We note that, due to the small equivalent widths of the Mg II 2796 Å transition in each case, no additional absorption lines are detected above the 3σ threshold at the same redshift, making the absorption identifications less certain than the higher equivalent width Mg II systems previously discussed. However, both of these systems exhibit absorption with 1σ significance at the expected location of the 2803 Å transition of the Mg II doublet, suggesting that despite the weakness of the features the detections are real. As shown in Figure 3, the equivalent widths and impact parameters measured for these absorbing galaxies also agree well with the previously determined relations at lower redshift.

The galaxy identified as G-5 has a well-identified Hα emission line in its G141 spectrum, with a luminosity implying an SFR $= 1.2\ M_\odot\ \mathrm{yr}^{-1}$. Galaxy G-6 exhibits no observable emission lines, despite having a narrowly determined redshift, which is primarily driven by the broadband photometry. The SPS modeling of its SED implies an SFR $\sim 0.1\ M_\odot\ \mathrm{yr}^{-1}$, consistent with the lack of Hα emission. Both galaxies fall well below the ΣSFR threshold believed to launch large-scale winds. Given the large projected distances at which the Mg II is observed around these galaxies, it is possible that the enriched gas was launched during a burst of star formation as much as 300 Myr earlier.

While the lower redshift absorption features are not the focal point of this work, it is interesting to note that their Mg II host galaxies, which coincidentally are detected at larger impact parameters (∼100 kpc) relative to the quasar sight line, exhibit a seemingly wider range in SFRs but similar stellar masses. Numerous studies at $z \lesssim 1$ have reported the detection of Mg II around galaxies with a diverse range of morphological and spectral types (e.g., Steidel et al. 1994), including quiescent galaxies, similar to G-6 (e.g., Gauthier & Chen 2011). Hence, the apparent host diversity we find is not unusual.

4.2. The Spatial Distribution of Mg II Around Galaxies

The inverse relationship between Mg II absorption equivalent width and galaxy impact parameter assumed in the survey design of Bouché et al. (2012b) is well established in the low- and intermediate-redshift universe (e.g., Lanzetta & Bowen 1990; Chen et al. 2010a, 2010b) and has been argued to drive the strong observed correlation between Mg II equivalent width and dust extinction in background quasars (Ménard et al. 2008). A tight inverse relation of W_r and ρ could also explain the strong correlation between Mg II equivalent width and [O II] emission observed in stacks of SDSS absorption spectra (Ménard et al. 2011).

Significant evolution in the observed scaling of the W_r–ρ relation could result in the non-detection of Mg II host galaxies in surveys with a limited field of view (e.g., Bouché et al. 2007, 2012b). While our data set is small, its unbiased selection and completeness enable us to look for any obvious departures from these scaling relations at lower redshift. In Figure 3, we compare our measurements at $z \sim 1.5$ to those in the largest existing

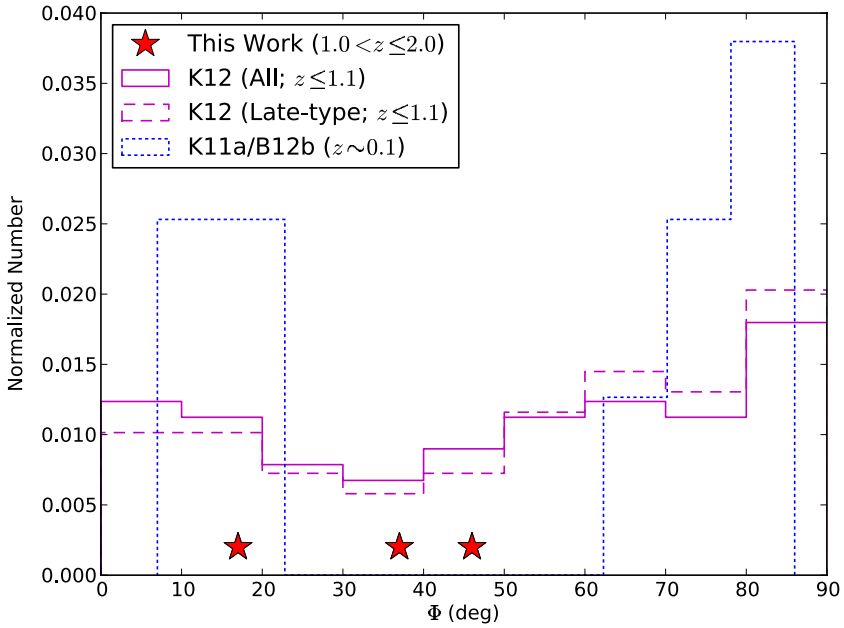

Figure 4. Distribution of the azimuthal angle (Φ) of galaxies, relative to the quasar sight lines in which Mg II absorption is detected at $W_r > 0.1$ Å. We compare our three individual high-redshift measurements of Φ (stars) with an ensemble of observations from two surveys at lower redshift. The lowest redshift data from Kacprzak et al. (2011a) and Bouché et al. (2012a) consist of 11 galaxy–absorber pairs at $z \sim 0.1$. The intermediate-redshift data from Kacprzak et al. (2012) include 88 galaxy–absorber pairs drawn from a compilation of studies (Chen et al. 2010a; Kacprzak et al. 2011a, 2011b; Churchill et al. 2012), shown in full (solid) and for late-type galaxies only (dashed). The data hint at an evolving azimuthal distribution of gas contained in outflows and traced by Mg II, which is consistent with the observed evolution in the collimation of outflows from star-forming galaxies from $z \sim 3$ (Law et al. 2012b).

(A color version of this figure is available in the online journal.)

low- and intermediate-redshift surveys (Chen et al. 2010a, 2010b; Kacprzak et al. 2011a, 2011b). While our observations appear to skirt the upper edge of the measurements from the absorber-blind survey of Chen et al. (2010a, 2010b), they agree quite well with the absorption-selected galaxy observations of Kacprzak et al. (2011a, 2011b). Thus, we find no signs of dramatic evolution in this relation from $z \sim 1.5$.

The various recent studies linking strong Mg II absorbers to star-forming galaxies at intermediate redshifts suggest that a substantial fraction of these absorbers originate in star-formation-driven winds. As such outflows are expected to propagate parallel to the minor axis of galaxies (e.g., Strickland et al. 2004), a signature of a wind-driven origin is expected in the azimuthal distribution of absorbers around galaxies. The first compelling evidence of the preferential distribution of strong Mg II along the minor axis of star-forming galaxies was reported in the stacked absorption line profiles of intermediate-redshift galaxies in zCOSMOS (Bordoloi et al. 2011). Using deep *HST* images to resolve the morphologies and position angles of individual Mg II galaxies, Kacprzak et al. (2012) confirmed a bimodal azimuthal distribution of Mg II absorption in the halos of $z \sim 0.5$ host galaxies, finding that the bulk of these absorbers are aligned within 20° of the major or minor axis of the host. Investigating a sample of 10 quasar–galaxy pairs, Bouché et al. (2012a) report an even more striking bimodality at $z \sim 0.1$. However, some of this difference could be attributed to the more stringent selection of inclined disk-dominated galaxies and higher cut on W_r in the Bouché et al. (2012a) analysis.

To investigate the persistence of this azimuthal dependence at higher redshift, we examine the spatial distribution of the Mg II absorption around the $z > 1$ galaxies in this work. In Figure 4, we compare our measurements to the azimuthal distributions of absorber–galaxy pairs with $W_r > 0.3$ Å from Bouché et al. (2012a) and $W_r > 0.1$ Å from Kacprzak et al. (2012). While the size of our sample limits what significant conclusions may be drawn from the distribution of Φ in this analysis, our data are the first measurements of this kind above $z \sim 1$ and therefore merit discussion.

At $1 < z < 2$, we find that the azimuthal angles (Φ, previously defined in Section 3.2.2) range from 17° to 46° with a typical uncertainty of 7°. One-third of the absorbers in our sample have an azimuthal angle within 20° of the major axis, precisely in agreement with the observations of Kacprzak et al. (2012), who suggest that this minority of absorbers can be explained by gas accretion occurring parallel to the major axes of the galaxies. However, 2/3 of our detections are found with $30° < \Phi < 60°$. This places our remaining absorbers outside the angular window ($\Phi > 60°$) within which the bulk of Mg II has been shown to inhabit at $z < 1$, particularly around star-forming galaxies (Bordoloi et al. 2011; Kacprzak et al. 2012) and at low redshift (Bouché et al. 2012a). While this azimuthal distribution might be considered as evidence opposing a wind-driven origin of the absorbing gas, the ultra-strong Mg II equivalent widths and large physical separations of these systems are difficult to reconcile with other origin scenarios.

The collimation of outflows along the minor axis of galaxies observed in local starbursts (e.g., Heckman et al. 1990; Lehnert & Heckman 1996; Cecil et al. 2001; Strickland & Heckman 2009) implies a correlation between the inclination of galaxies and their wind velocities, which can be measured using the blueshifts of low-ionization absorption features of galaxies hosting outflows. This correlation has been observed locally, where galaxy morphologies are readily resolved (Heckman et al. 2000; Chen et al. 2010), and with deep multi-band imaging at $z = 1$ (Kornei et al. 2012). However, observations at higher redshift ($z = 1.4$) by Weiner et al. (2009) failed to reproduce

the relation, possibly due to the difficulty of resolving galaxy morphologies at higher redshift, even with *HST I*-band imaging.

A recent study by Law et al. (2012b) incorporated deep *HST* WFC3/IR imaging to better resolve the rest-frame optical morphologies of star-forming galaxies at $z > 2$. Their findings indicate that the correlation between outflow velocity and inclination is indeed absent in low-mass galaxies at $z \sim 2$–3, suggesting that the typically more irregular and "puffy" high-redshift galaxies have poorly collimated outflows. This increasing collimation of star-formation-driven winds with redshift is an expected result of galaxies evolving with time from low-mass dispersion-dominated systems to more massive, stable disks.

If the typical geometry of star-formation-driven outflows evolves with time to become highly collimated in the local universe, a signature of this evolution should be expected in the azimuthal distribution of metal-enriched gas in the circumgalactic medium surrounding star-forming galaxies. Despite the small sample size, our data are consistent with an evolutionary trend in which the collimation of galaxy-scale outflows increases with time. Moreover, the fact that the typical halo masses of Mg II host galaxies appear not to evolve from $z \sim 2$ suggests that the trend of increasing collimation with time holds for star-forming galaxies at constant mass (i.e., the outflows of star-forming galaxies with $\log(M_*/M_\odot) = 9.75$ are randomly oriented at $z > 2$ and more tightly collimated at lower z). We stress that a more extensive survey of Mg II host galaxies with *HST* would be required to determine the significance of this finding.

4.3. Absorption Properties of All Proximate Galaxies

In a parallel search for absorption around all 3D-HST galaxies identified within 150 kpc of the quasar sight line, we detect eight galaxies with well-determined redshifts in the range $0.65 < z < 2.6$. We provide the SED and redshift probability density function, $P(z)$, for each galaxy in Figure 5. All four of the galaxies with $z > 0.9$ are coincidentally located within 60 kpc of the quasar sight line, while the galaxies with lower redshifts are detected at larger impact parameters. The separations in the redshifts of these objects ensure that there is no physical correlation between any of these galaxies or with the quasar. Thus, the apparent angular clustering of high-redshift galaxies around the quasar sight line should be understood simply as a coincidence and not distract from the other underlying physical correlations of absorbers and host galaxies in this study.

Three of the four galaxies with $\rho < 60$ kpc exhibit Mg II absorption with $W_r > 0.8$ Å, as discussed at length in Section 4.1. The remaining galaxy within this radius is undetected in Mg II to our observational limit of $W_r > 0.4$ Å. Of the galaxies detected in absorption, all have SFR $> 4\,M_\odot$ yr^{-1} and ΣSFR $> 0.3\,M_\odot$ yr^{-1} kpc^{-2}, uncorrected for dust extinction. The remaining galaxy, G-4, which is undetected in absorption at a similarly close separation of 53 kpc, exhibits no measurable emission lines in the G141 data at the best-fit combined grism/photometric redshift of 0.952. Although we only measure an upper limit for the Hα emission in the 1D grism spectrum ($W_r \sim 6$ Å), SPS modeling of the SED results in an SFR $\sim 2\,M_\odot$ yr^{-1}.

The possibility remains that the best-fit photometric redshift for G-4 could be incorrect, which might simultaneously explain the lack of emission lines in the G141 spectra and the absence of Mg II absorption in the quasar spectra where they are expected. However, the redshift probability distribution function derived from the SED of the galaxy indicates a <1% probability that the observable wavelength of Hα emission lies outside of the range of the G141 spectrum. Thus, the fact that we find no strong evidence for vigorous ongoing star formation in the only galaxy within 60 kpc that is undetected in Mg II absorption suggests that the SFR of the host galaxy is indeed correlated with the large-scale distribution of cold gas in the circumgalactic medium.

Taken together, our data indicate that the covering fraction (f_c) of cold gas with $W_r^{\lambda 2796} > 0.8$ Å may be as large as unity to at least 60 kpc around star-forming galaxies at $1 \lesssim z \lesssim 2$. Given the small number of objects available for this study, we are unable to place tight constraints on these measurements. However, it is interesting to note that this covering fraction estimate is quite high relative to measurements at lower redshift. A recent examination of the Mg II absorption properties of galaxies in the DEEP2 survey estimated $f_c = 0.5$ around typical galaxies at $z = 1$ (Lundgren et al. 2011). At $z = 0.5$, the typical covering fraction varies from $f_c = 0.25$ to $f_c = 1$, depending on the chosen limits of Mg II equivalent width and impact parameter (Bergeron & Boissé 1991; Bechtold & Ellingson 1992; Steidel et al. 1994; Tripp & Bowen 2005). In the local universe, f_c appears to drop below 0.25 for all galaxies (Barton & Cooke 2009), but remains high among those with high SFRs (Bowen et al. 1995). Thus, we seem to be observing a trend of a declining mean f_c with time. This is, of course, what one might expect given the fact that the global SFR density is also dropping dramatically from $z \sim 2$. As the fraction of galaxies with halos rich in cold gas is depleted with time, the average f_c should also be expected to decline.

If we include all galaxies detected within 150 kpc in this study, regardless of redshift or SFR, we estimate that the covering fraction for $W_r^{2796} > 0.2$ Å is $f_c(60\text{ kpc}) = 0.75$, $f_c(100\text{ kpc}) = 0.66$, and $f_c(150\text{ kpc}) = 0.63$.

5. SUMMARY

By exploiting the only known bright $z > 2$ quasar within the 3D-HST Survey area, we have analyzed the $W_r^{\lambda 2796} > 0.2$ Å metal absorption properties of a small but complete sample of spectroscopically confirmed galaxies with $H_{140} \gtrsim 24$ at $0.65 < z < 2$. The unique depth and resolution of the WFC3 observations have enabled an examination of the host galaxies of quasar absorption lines over a range of impact parameters and SFRs previously unavailable at high redshift, and the slitless nature of the G141 grism ensures a nearly complete redshift census of galaxies proximate to the quasar sight line. Thus, our analysis avoids the most prohibitive selection biases of previous studies of absorber host galaxies at $z > 1$.

We unambiguously detect an isolated host galaxy for each of the three multi-ion absorption line systems detected with $W_r^{\lambda 2796} > 0.8$ Å along the line of sight to quasar SDSS J123622.93+621526.6. The galaxies occupy the redshift range $1 < z < 2$ and have SFRs in excess of $4\,M_\odot$ yr^{-1}. In each case the ΣSFR $> 0.3\,M_\odot$ yr^{-1} kpc^{-2}, exceeding $0.1\,M_\odot$ yr^{-1} kpc^{-2}, the threshold for local starburst galaxies.

The three absorber host galaxies have a mean stellar mass of $\log(M_*/M_\odot) \sim 9.75$, consistent with the typical dark matter halo masses derived from clustering measurements of Mg II absorbers at $z \lesssim 1$. The F140W morphologies of the host galaxies indicate a wide range in Sérsic indices, and profiles consistent with the compact triaxial systems and thick disks commonly observed among similarly low-mass galaxies at $z \gtrsim 2$.

We observe no strong evolution in the relation between Mg II equivalent width and impact parameter from $z \sim 2$. However, the spatial distribution of the high-redshift Mg II

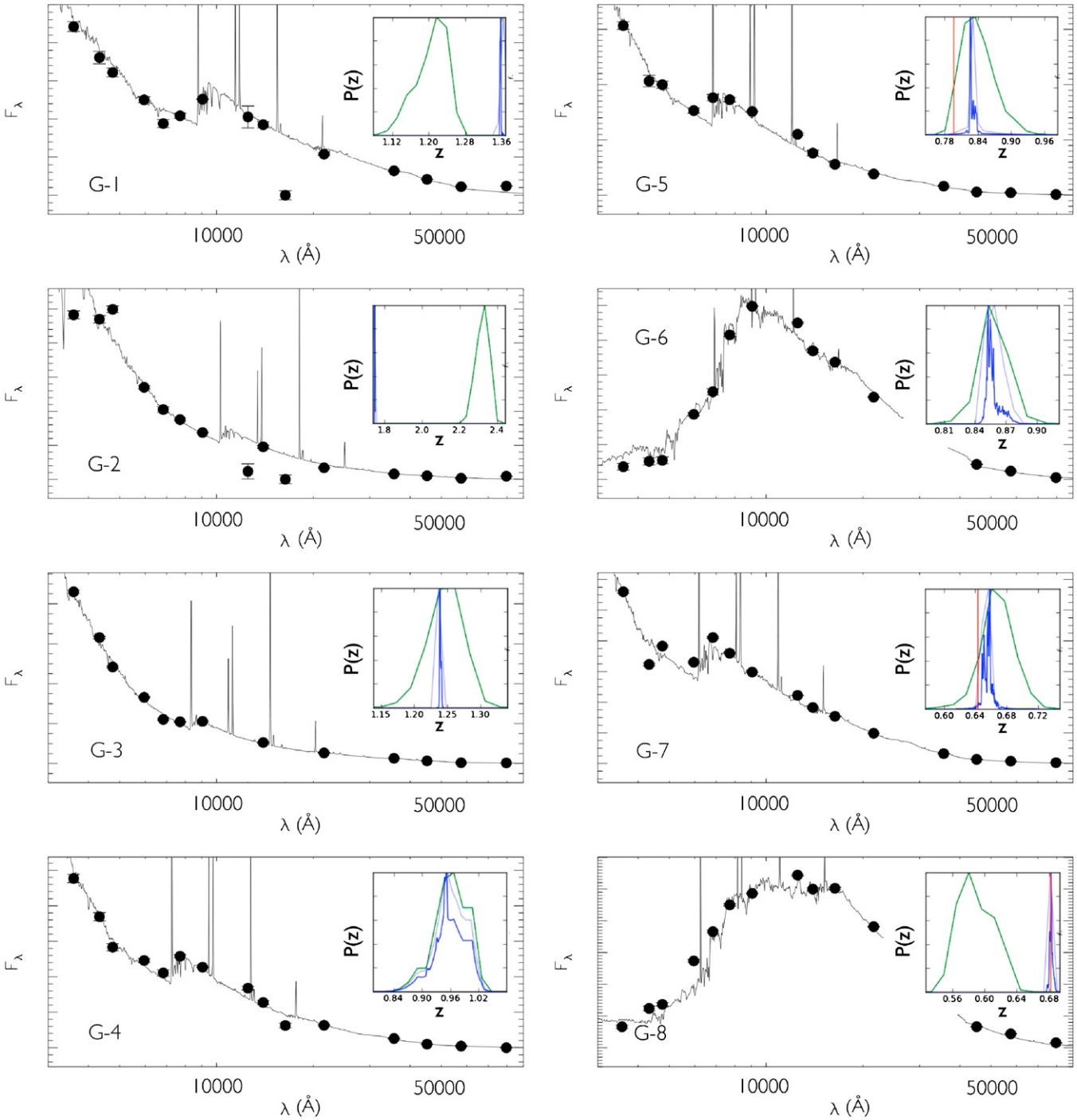

Figure 5. Broadband SEDs of the eight galaxies identified within 150 kpc of the quasar sight line, provided with arbitrary units of F_λ. In each case the best-fit galaxy template, fitted to the redshift determined from the grism spectrum, is overplotted. Black dots represent the broadband photometric measurements detailed in Table 1. Redshift probability distribution functions, $P(z)$, are inset within each panel. The green curve provides the broadband photometric solution of the $P(z)$. The blue curve provides the $P(z)$ determined from the G141 data. Red vertical lines in panels G-5, G-7, and G-8 indicate the spectroscopic redshifts reported by Barger et al. (2008).
(A color version of this figure is available in the online journal.)

absorption around the host galaxies appears to have a weaker azimuthal dependence than studies at $z \lesssim 1$ (Bouché et al. 2012a; Kacprzak et al. 2012), indicating possible evolution in the angular distribution of high-W_r Mg II absorption in galaxy halos. Though a larger statistical sample would be required to confirm this behavior, these results are consistent with the recent findings of an increasing collimation of star-formation-driven outflows with time from $z \sim 3$, resulting from the evolution of low-mass star-forming galaxies from dispersion-dominated triaxial systems to stable disks (Law et al. 2012b).

By examining the $W_r > 0.2$ Å absorption properties of all galaxies detected in 3D-HST within 150 kpc of the quasar sight line, we measure the typical covering fraction of Mg II-enriched gas at $z > 0.65$ to be $f_c = 0.75$ at $\rho < 60$ kpc, $f_c = 0.66$ at

$\rho < 100$ kpc, and $f_c = 0.63$ at $\rho < 150$ kpc. In addition, we find that the $W_r > 0.8$ Å covering fraction is approximately unity to at least 60 kpc around star-forming galaxies at $1 < z < 2$.

Looking toward future work, we note that this analysis would greatly benefit from WFC3/IR follow-up of additional fields around absorber-rich sight lines. The vast quasar catalogs available from the SDSS (York et al. 2000; Schneider et al. 2010) and the SDSS-III Baryon Oscillation Spectroscopic Survey (Eisenstein et al. 2011; Ross et al. 2012; I. Paris et al. 2012, submitted) are producing unprecedented numbers of metal absorption line systems (e.g., D. G. York et al., in preparation). Targeting the densest of these sight lines with *HST* would likely provide the numbers of absorber–galaxy pairs to better constrain the evolution hinted at in this analysis.

This work would not have been possible without the publicly available data from the Sloan Digital Sky Survey, the Team Keck Redshift Survey, and from the GOODS-N grism program GO-11600 (PI: Benjamin Weiner). We are grateful to Nicholas Bouché, Glenn Kacprzak, Nikole Nielson, and Jason Tumlinson for helpful discussions. We also thank the anonymous referee for providing a detailed report which has improved the clarity of the text. Support from HST grant GO-12177 is gratefully acknowledged. We also acknowledge funding from ERC grant HIGHZ No. 227749. This work is based on observations taken by the 3D-HST Treasury Program with the NASA/ESA *HST*, which is operated by the Association of Universities for Research in Astronomy, Inc., under NASA contract NAS5-26555. This research has made extensive use of NASA's Astrophysics Data System Bibliographic Services and of open source scientific Python libraries, including PyFITS and PyRAF produced by the Space Telescope Science Institute, which is operated by AURA for NASA.

REFERENCES

Barton, E. J., & Cooke, J. 2009, AJ, 138, 1817
Bahcall, J. N., & Spitzer, L., Jr. 1969, ApJ, 156, L63
Barger, A. J., Cowie, L. L., & Wang, W.-H. 2008, ApJ, 689, 687
Bechtold, J., & Ellingson, E. 1992, ApJ, 396, 20
Bergeron, J., & Boissé, P. 1991, A&A, 243, 344
Bertin, E., & Arnouts, S. 1996, A&AS, 117, 393
Bordoloi, R., Lilly, S. J., Knobel, C., et al. 2011, ApJ, 743, 10
Bouché, N., Hohensee, W., Vargas, R., et al. 2012a, MNRAS, 426, 801
Bouché, N., Murphy, M. T., Péroux, C., Csabai, I., & Wild, V. 2006, MNRAS, 371, 495
Bouché, N., Murphy, M. T., Péroux, C., et al. 2007, ApJ, 669, L5
Bouché, N., Murphy, M. T., Péroux, C., et al. 2012b, MNRAS, 419, 2
Bowen, D. V., Blades, J. C., & Pettini, M. 1995, ApJ, 448, 634
Brammer, G. B., van Dokkum, P. G., & Coppi, P. 2008, ApJ, 686, 1503
Brammer, G., van Dokkum, P., Franx, M., et al. 2012, ApJS, 200, 13
Bruzual, G., & Charlot, S. 2003, MNRAS, 344, 1000
Capak, P., Cowie, L. L., Hu, E. M., et al. 2004, AJ, 127, 180
Cecil, G., Bland-Hawthorn, J., Veilleux, S., & Filippenko, A. V. 2001, ApJ, 555, 338
Chen, H.-W., Helsby, J. E., Gauthier, J.-R., et al. 2010a, ApJ, 714, 1521
Chen, H.-W., Wild, V., Tinker, J. L., et al. 2010b, ApJ, 724, L176
Chen, Y.-M., Tremonti, C. A., Heckman, T. M., et al. 2010, AJ, 140, 445
Chun, M. R., Kulkarni, V. P., Gharanfoli, S., & Takamiya, M. 2010, AJ, 139, 296
Churchill, C. W., Kacprzak, G. G., Steidel, C. C., et al. 2012, arXiv:1205.0595
Churchill, C. W., Mellon, R. R., Charlton, J. C., et al. 2000, ApJ, 543, 577
Conselice, C. J., Blackburne, J. A., & Papovich, C. 2005, ApJ, 620, 564
Crighton, N. H. M., Morris, S. L., Bechtold, J., et al. 2010, MNRAS, 402, 1273
Dickinson, M., Giavalisco, M., & GOODS Team, 2003, in The Mass of Galaxies at Low and High Redshift, ed. R. Bender & A. Renzini (Berlin: Springer), 324
Di Matteo, T., Springel, V., & Hernquist, L. 2005, Nature, 433, 604
Eisenstein, D. J., Weinberg, D. H., Agol, E., et al. 2011, AJ, 142, 72
Elmegreen, B. G., & Elmegreen, D. M. 2006, ApJ, 650, 644
Elmegreen, D. M., Elmegreen, B. G., Rubin, D. S., & Schaffer, M. A. 2005, ApJ, 631, 85
Erb, D. K., Quider, A. M., Henry, A. L., & Martin, C. L. 2012, arXiv:1209.4903
Faber, S. M., Phillips, A. C., Kibrick, R. I., et al. 2003, Proc. SPIE, 4841, 1657
Gauthier, J.-R., & Chen, H.-W. 2011, MNRAS, 418, 2730
Gauthier, J.-R., Chen, H.-W., & Tinker, J. L. 2009, ApJ, 702, 50
Genzel, R., Burkert, A., Bouché, N., et al. 2008, ApJ, 687, 59
Genzel, R., Tacconi, L. J., Eisenhauer, F., et al. 2006, Nature, 442, 786
Giavalisco, M., Ferguson, H. C., Koekemoer, A. M., et al. 2004, ApJ, 600, L93
Häussler, B., McIntosh, D. H., Barden, M., et al. 2007, ApJS, 172, 615
Heckman, T. M. 2002, in ASP Conf. Proc. 254, Extragalactic Gas at Low Redshift, ed. J. S. Mulchaey & J. Stocke (San Francisco, CA: ASP), 292
Heckman, T. M., Armus, L., & Miley, G. K. 1990, ApJS, 74, 833
Heckman, T. M., Lehnert, M. D., Strickland, D. K., & Armus, L. 2000, ApJS, 129, 493
Hopkins, P. F., Hernquist, L., Cox, T. J., et al. 2005, ApJ, 630, 705
Kacprzak, G. G., Churchill, C. W., Barton, E. J., & Cooke, J. 2011a, ApJ, 733, 105
Kacprzak, G. G., Churchill, C. W., Ceverino, D., et al. 2010, ApJ, 711, 533
Kacprzak, G. G., Churchill, C. W., Evans, J. L., Murphy, M. T., & Steidel, C. C. 2011b, MNRAS, 416, 3118
Kacprzak, G. G., Churchill, C. W., & Nielsen, N. M. 2012, arXiv:1205.0245
Kajisawa, M., Ichikawa, T., Tanaka, I., et al. 2011, PASJ, 63, 379
Kennicutt, R. C., Jr. 1998, ApJ, 498, 541
Kornei, K. A., Shapley, A. E., Martin, C. L., et al. 2012, arXiv:1205.0812
Kriek, M., van Dokkum, P. G., Labbé, I., et al. 2009, ApJ, 700, 221
Lanzetta, K. M., & Bowen, D. 1990, ApJ, 357, 321
Law, D. R., Steidel, C. C., Shapley, A. E., et al. 2012a, ApJ, 745, 85
Law, D. R., Steidel, C. C., Shapley, A. E., et al. 2012b, arXiv:1206.6889
Le Brun, V., Bergeron, J., Boisse, P., & Christian, C. 1993, A&A, 279, 33
Lehnert, M. D., & Heckman, T. M. 1996, ApJ, 462, 651
Lundgren, B. F., Brunner, R. J., York, D. G., et al. 2009, ApJ, 698, 819
Lundgren, B. F., Wake, D. A., Padmanabhan, N., Coil, A., & York, D. G. 2011, MNRAS, 417, 304
Lundgren, B. F., van Dokkum, P., Franx, M., et al. 2012, ApJ, submitted
Madau, P., Ferrara, A., & Rees, M. J. 2001, ApJ, 555, 92
Martin, C. L., Shapley, A. E., Coil, A. L., et al. 2012, arXiv:1206.5552
Ménard, B., Nestor, D., Turnshek, D., et al. 2008, MNRAS, 385, 1053
Ménard, B., Wild, V., Nestor, D., et al. 2011, MNRAS, 417, 801
Nelson, E. J., van Dokkum, P. G., Brammer, G., et al. 2012, ApJ, 747, L28
Nestor, D. B., Johnson, B. D., Wild, V., et al. 2011, MNRAS, 412, 1559
Nestor, D. B., Turnshek, D. A., & Rao, S. M. 2005, ApJ, 628, 637
Nestor, D. B., Turnshek, D. A., Rao, S. M., & Quider, A. M. 2007, ApJ, 658, 185
Norman, C. A., Bowen, D. V., Heckman, T., Blades, C., & Danly, L. 1996, ApJ, 472, 73
Noterdaeme, P., Srianand, R., & Mohan, V. 2010, MNRAS, 403, 906
Nulsen, P. E. J., Barcons, X., & Fabian, A. C. 1998, MNRAS, 301, 168
Peng, C. Y., Ho, L. C., Impey, C. D., & Rix, H.-W. 2002, AJ, 124, 266
Prochaska, J. X., & Wolfe, A. M. 1997, ApJ, 487, 73
Prochter, G. E., Prochaska, J. X., & Burles, S. M. 2006, ApJ, 639, 766
Quider, A. M., Nestor, D. B., Turnshek, D. A., et al. 2011, AJ, 141, 137
Ravindranath, S., Giavalisco, M., Ferguson, H. C., et al. 2006, ApJ, 652, 963
Ross, N. P., Myers, A. D., Sheldon, E. S., et al. 2012, ApJS, 199, 3
Rubin, K. H. R., Weiner, B. J., Koo, D. C., et al. 2010, ApJ, 719, 1503
Salpeter, E. E. 1955, ApJ, 121, 161
Sanders, D. B., Soifer, B. T., Elias, J. H., et al. 1988, ApJ, 325, 74
Scannapieco, E., Ferrara, A., & Madau, P. 2002, ApJ, 574, 590
Schneider, D. P., Richards, G. T., Hall, P. B., et al. 2010, AJ, 139, 2360
Steidel, C. C., Adelberger, K. L., Shapley, A. E., et al. 2003, ApJ, 592, 728
Steidel, C. C., Dickinson, M., Meyer, D. M., Adelberger, K. L., & Sembach, K. R. 1997, ApJ, 480, 568
Steidel, C. C., Dickinson, M., & Persson, S. E. 1994, ApJ, 437, L75
Steidel, C. C., Erb, D. K., Shapley, A. E., et al. 2010, ApJ, 717, 289
Stewart, K. R., Kaufmann, T., Bullock, J. S., et al. 2011, ApJ, 735, L1
Straka, L. A., Kulkarni, V. P., York, D. G., Woodgate, B. E., & Grady, C. A. 2010, AJ, 139, 1144
Strickland, D. K., & Heckman, T. M. 2009, ApJ, 697, 2030
Strickland, D. K., Heckman, T. M., Colbert, E. J. M., Hoopes, C. G., & Weaver, K. A. 2004, ApJS, 151, 193
Tinker, J. L., & Chen, H.-W. 2008, ApJ, 679, 1218
Tripp, T. M., & Bowen, D. V. 2005, in IAU Colloq. 199: Probing Galaxies through Quasar Absorption Lines, ed. P. R. Williams, C.-G. Shu, & B. Menard (Cambridge: Cambridge Univ. Press), 5

Uomoto, A., Smee, S., Rockosi, C., et al. 1999, BAAS, 31, 1501
van Dokkum, P. G., Brammer, G., Fumagalli, M., et al. 2011, ApJ, 743, L15
Wake, D. A., Whitaker, K. E., Labbé, I., et al. 2011, ApJ, 728, 46
Weiner, B. J., Coil, A. L., Prochaska, J. X., et al. 2009, ApJ, 692, 187
Wirth, G. D., Willmer, C. N. A., Amico, P., et al. 2004, AJ, 127, 3121
Wuyts, S., Förster Schreiber, N. M., Lutz, D., et al. 2011, ApJ, 738, 106
York, D. G., Adelman, J., Anderson, J. E., Jr., et al. 2000, AJ, 120, 1579
York, D. G., vanden Berk, D., Richards, G. T., et al. 2005, in IAU Colloq. 199: Probing Galaxies through Quasar Absorption Lines, ed. P. R. Williams, C.-G. Shu, & B. Menard (Cambridge: Cambridge Univ. Press), 58
Zibetti, S., Ménard, B., Nestor, D. B., Quider, A. M., & Rao, S. M. 2007, ApJ, 658, 161